Electronic Supplementary Material (ESI) for Journal of Materials Chemistry C.


# $MoS_2$ mediated tuning of $CuCo_2S_4$-$MoS_2$ nanocomposites for high-performance symmetric hybrid supercapacitors†

Mohasin Tarek and M. A. Basith*

*Nanotechnology Research Laboratory, Department of Physics, Bangladesh University of Engineering and Technology, Dhaka-1000, Bangladesh.*

E-mail: mabasith@phy.buet.ac.bd

# Electronic Supporting Information (ESI)

## Note S1. Synthesis method

### Synthesis of Nanostructured $CuCo_2S_4$

The low temperature hydrothermal synthesis technique was used to produce nanostructured CCS [1]. Initially, a 50 mL 1:1 (v/v) ethanol and deionized (DI) water solution was prepared to dissolve 1 mmol $Cu(NO_3)_2.3H_2O$, 2 mmol $Co(NO_3)_2.6H_2O$, and 4 mmol of $CH_4N_2S$. After magnetically stirring the mixture for one hour, a pink homogeneous solution was obtained. Subsequently, $NH_4OH$ was added dropwise while stirring, until the pH reached 10. The resulting solution was then transferred to a Teflon-lined stainless steel autoclave and subjected to heating at 180 °C for 12 hours, followed by natural cooling to room temperature.

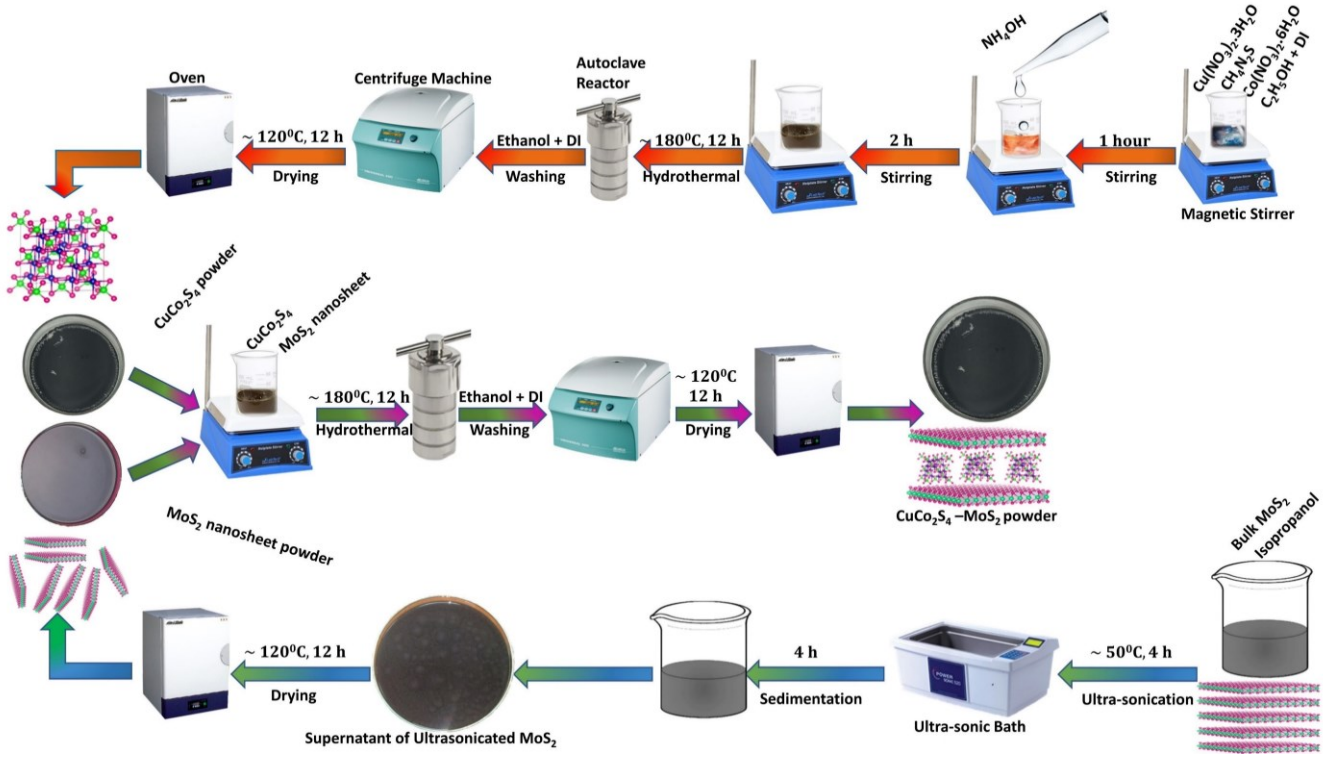


**Fig. S1.** Schematically the syntheses steps of $CuCo_2S_4$ by hydrothermal technique, $MoS_2$ nanosheets via ultrasonication and $CuCo_2S_4$-$MoS_2$ nanocomposites using also hydrothermal technique.

The final product underwent multiple washes in DI water and ethanol to get rid of all traces of solvent. Finally, the product is dried in an oven at 120 °C temperature to yield nanostructured CCS [1].

### Synthesis of $MoS_2$ nanosheets

$MoS_2$ NSs were synthesized using an ultrasonication-assisted exfoliation technique from bulk $MoS_2$ powder [1,2]. Initially 500 mg of $MoS_2$ powder was dissolved in 100 ml of isopropanol. After that, the solution was ultrasonicated in an ultrasonic bath at 50 °C for four hours. Subsequently, the sonicated solution was left undisturbed for 4 hours to enable the precipitation of a powdery residue and thick sheets at the micron scale. The supernatant was isolated as $MoS_2$ nanosheets after sedimentation. Finally, the obtained supernatant was placed in an oven and dried at 120 °C for 12 h to extract the powdered $MoS_2$ nanosheets (NSs) [1,2].

### Synthesis of $CuCo_2S_4$-$MoS_2$ Nanocomposites

A simple hydrothermal synthesis method was again used to synthesize the CCS-$MoS_2$ nanocomposite of previously prepared nanostructured CCS and $MoS_2$ NSs [1]. For CCS-$MoS_2$ (85:15) nanocomposite, firstly, 50 mL of DI water was used to dissolve 33 mg of $MoS_2$ NSs and 187 mg of CCS. This mixture was magnetically stirred for three hours. The solution was then placed in an autoclave and heated to 180 °C for 12 hours before being allowed to cool to room temperature. The next step was centrifugation, followed by DI water and ethanol wash. Finally, CCS-$MoS_2$ was obtained by drying the filtered solution at 120 °C temperature in an oven for 12 hours. The above-mentioned method was used to prepare CCS-$MoS_2$ nanocomposites with $MoS_2$ inclusions at 20, 25 and 30 wt%.

## Note S2. Preparation of Working Electrodes

Both the three-electrode and symmetric two-electrode setups employed a 0.5 M $Na_2SO_4$ aqueous solution as the electrolyte. In the three-electrode system, the reference electrode was an Ag/AgCl electrode immersed in saturated KCl solution, while the counter electrode was a platinum wire. To prepare the working electrode, 20 mg of the synthesized active material (90 wt%) was sonicated with 2.22 mg of polyvinylidene fluoride (PVDF; 10 wt%) as a binder and 200 $\mu$L of N-methyl-2-pyrrolidone (NMP) as a solvent for 2 hours. This produced a homogeneous slurry of electrode materials. The slurry was then uniformly cast onto a graphite rod with a surface area of 0.28 $cm^2$. The modified graphite rod was subsequently dried at 100 °C for 12 hours, ensuring the formation of a three-electrode cell's working electrode. Following the three-electrode setup, the symmetric two-electrode configuration was established. The previously prepared active material slurry was cast onto two graphite rods, with equal amounts of slurry applied to each graphite rod. These modified graphite rods were utilized as the anode and cathode in the symmetric two-electrode arrangement.

## Note S3. Electrochemical Measurement

To calculate the capacitance ($C_{cell}$ in F), specific capacitance ($C_{sp}$ in F $g^{-1}$ unit) from the CV and GCD in the three-electrode system (or half cells), we employed Eq. 1, 2 and 3, respectively [1,3-5].

$$C_{\text{cell}} = \frac{I\Delta t}{\Delta V} \tag{1}$$

$$C_{sp} = \frac{\int J\Delta V}{2\nu\Delta V} \tag{2}$$

$$C_{sp} = \frac{J\Delta t}{\Delta V} \tag{3}$$

$$J = \frac{I}{m} \tag{4}$$

Where, J, m, $\Delta t$, $\Delta V$ and $\nu$ stand for current density, mass of active material, time to discharge, potential window, and scan rate, respectively.

The capacitance ($C_{cell}$) that arises when a voltage is applied between the two electrodes can be represented using the following formula:

$$\frac{1}{C_{\text{cell}}} = \frac{1}{C_{+}} + \frac{1}{C_{-}} \tag{5}$$

where $C_{cell}$, $C_+$, and $C_-$ are the capacitance (in Farad) of the resulting device or cell, of the positive electrode, and of the negative electrode, respectively. With the capacitance ($C_{cell}$) determined from the GCD profile using Eq. 1 In a symmetrical system, where both the positive and negative electrodes have similar morphological and electronic characteristics ($C_+ = C_-$), the cell capacitance ($C_{cell}$) can be calculated as per the following equations provided in Eq. 5.

$$C_{\text{cell}} = \frac{C}{2} \tag{6}$$

where $C = C_+ = C_-$. The electrode capacitance is calculated using the following equation:

$$C = 2 \times C_{\text{cell}} \tag{7}$$

In the realm of electrochemical supercapacitors, for the sake of comparing various electrode materials, it is a standard procedure to determine the specific capacitance ($C_{sp}$), which is associated with the capacitance of a single electrode and is expressed in F $g^{-1}$. Consequently, by dividing Eq. 7 by the mass of an individual electrode m, we can apply Eq. 8.

$$C_{\text{sp}} = \frac{2 \times C_{\text{cell}}}{m} \tag{8}$$

Where m (g) is the mass of the single electrode. For a symmetric system, the specific capacitance of the single electrode ($C_{sp}$) is given by:

$$C_{sp} = \frac{4C_{\text{cell}}}{m} \tag{9}$$

The 'M' represents the combined mass of the active materials in both electrodes, which is equal to 2 times 'm' since each electrode has the same weight. The factor of 4 serves as an adjustment, aligning the cell capacitance and the combined weight of the two electrodes with the capacitance and mass of a single electrode.

However, the specific capacitance ($C_{sp}$ in F $g^{-1}$ unit), specific energy density ($E_{sp}$ in W h $kg^{-1}$ unit), and specific power density ($P_{sp}$ in W $kg^{-1}$ unit) of the symmetric two-electrode system (for single electrode) were calculated from GCD, using Eq. 10, 11, and 12, respectively [6,7]. or

$$C_{sp} = \frac{4J\Delta t}{\Delta V} \tag{10}$$

$$E_{sp} = \frac{C_{sp}(\Delta V)^2 \times 1000}{8 \times 3600} \tag{11}$$

$$P_{sp} = \frac{E_{sp} \times 3600}{\Delta t} \tag{12}$$

Where, m is the total mass of the active material (both anode and cathode electrode). Using CV analysis, one may infer the charge storage mechanism. Eq. 13 (Tefel's equation) was

employed for this purpose. The logarithm of both sides of Eq. 13 yields Eq. 14 [8-10].

$$I = a\nu^b \tag{13}$$

$$log(I) = blog(\nu) + log(a) \tag{14}$$

Where, I is the working electrode current (when V = 0 V), $\nu$ is the scan rate, and b is the slope. To estimate the value of slope "b", the graph of ($\log I \sim \log \nu$) was plotted (which was straight line). The charge storage mechanism depends on the value of this slope "b". The value of "b" equal to 0.5 represents the Faradic interrelation process, 1 the EDL capacitance method, and $0.5 < b < 1$ the combination of the two techniques. At a particular scan rate and potential difference, Eq. 15 provides the capacitive resultant current as well as the diffusion controlled resultant current [8-10].

$$I(V) = k_1\nu + k_2\nu^{\frac{1}{2}} \tag{15}$$

$$\frac{I(V)}{\nu^{\frac{1}{2}}} = k_1\nu^{\frac{1}{2}} + k_2 \tag{16}$$

In Eq. 11, $k_1\nu$ represents the capacitive resultant current and $k_2\nu^{\frac{1}{2}}$ corresponds the resulting current in a diffusion-controlled system. Using Eq. 16, both $k_1$ and $k_2$ can be obtained from the slope and y-intercept of the ($\nu^{\frac{1}{2}} \sim \frac{I}{\nu^{\frac{1}{2}}}$) graph, respectively. In this case, the value of the current was taken at V = 0 V. Additionally, the impact of charge storage technique on the overall capacitance can be examined with Trasatti's approach. According to this approach, when $\nu$ = 0 mV $s^{-1}$, charge may be accessible at both the surface and the inner region of the electrode, indicating the total capacitance. Nevertheless, the EDL capacitance is only accessible when $\nu$ = infinity and the charge is confined to the electrode's surface. From ($\frac{1}{C_{\text{sp}}} \sim \nu^{\frac{1}{2}}$) and ($C_{\text{sp}} \sim \frac{1}{\nu^{\frac{1}{2}}}$) graphs, total capacitance ($C_T$) and EDL capacitance ($C_{EDL}$) can be determined by taking the y-intercepts using Eq. 18 and Eq. 20 respectively, and

pseudocapacitance ($C_{pseu}$) from Eq. 21 [11,12].

$$\frac{1}{C_{sp}} = constant \times \nu^{0.5} + \frac{1}{C_T} \tag{17}$$

$$C_T = \frac{1}{y\,intercept\,of(\frac{1}{C_{sp}} \sim \nu^{0.5})graph} \tag{18}$$

$$C_{sp} = constant \times \nu^{-0.5} + C_{EDL} \tag{19}$$

$$C_{EDL} = y\,intercept\,of(C_{sp} \sim \frac{1}{\nu^{0.5})}graph \tag{20}$$

$$C_{pseudo} = C_T - C_{EDL} \tag{21}$$

$$C_{EDL}(\%) = \frac{C_{EDL}}{C_T} \times 100\% \tag{22}$$

$$C_{pseudo}(\%) = \frac{C_{pseudo}}{C_T} \times 100\% \tag{23}$$

The percentages of $C_{EDL}$ and $C_{pseu}$ in the total capacitance can be calculated from Eq. 22 and Eq. 23, respectively.

**Table S1**. Crystallographic parameters for all the constituents of the as-synthesized nanomaterials obtained after Rietveld refinement.

| Sample | Constituent | Crystallographic phase | Space group | a(Å) | b(Å) | c(Å) | d-spacing (nm) | $\chi^2$ |
|---|---|---|---|---|---|---|---|---|
| $MoS_2$ nanosheets | $MoS_2$ | Hexagonal | *P 63/m m c* | 3.197 | 3.197 | 12.382 | 0.621 | 1.14 |
| $CuCo_2S_4$ | $CuCo_2S_4$ | Cubic | *F d -3 m* | 9.460 | 9.460 | 9.460 | 0.285 | 1.25 |
| $CuCo_2S_4$-$MoS_2$ (85:15) | $CuCo_2S_4$ | Cubic | *F d -3 m* | 9.546 | 9.546 | 9.546 | 0.291 | 2.09 |
| | $MoS_2$ | Hexagonal | *P 63/m m c* | 3.22 | 3.22 | 12.454 | 0.625 | |
| $CuCo_2S_4$-$MoS_2$ (80:20) | $CuCo_2S_4$ | Cubic | *F d -3 m* | 9.655 | 9.655 | 9.655 | 0.297 | 1.19 |
| | $MoS_2$ | Hexagonal | *P 63/m m c* | 3.30 | 3.30 | 12.502 | 0.632 | |
| $CuCo_2S_4$-$MoS_2$ (75:25) | $CuCo_2S_4$ | Cubic | *F d -3 m* | 9.574 | 9.574 | 9.574 | 0.294 | 2.5 |
| | $MoS_2$ | Hexagonal | *P 63/m m c* | 3.25 | 3.25 | 12.476 | 0.627 | |
| $CuCo_2S_4$-$MoS_2$ (70:30) | $CuCo_2S_4$ | Cubic | *F d -3 m* | 9.508 | 9.508 | 9.508 | 0.288 | 2.38 |
| | $MoS_2$ | Hexagonal | *P 63/m m c* | 3.20 | 3.20 | 12.427 | 0.622 | |

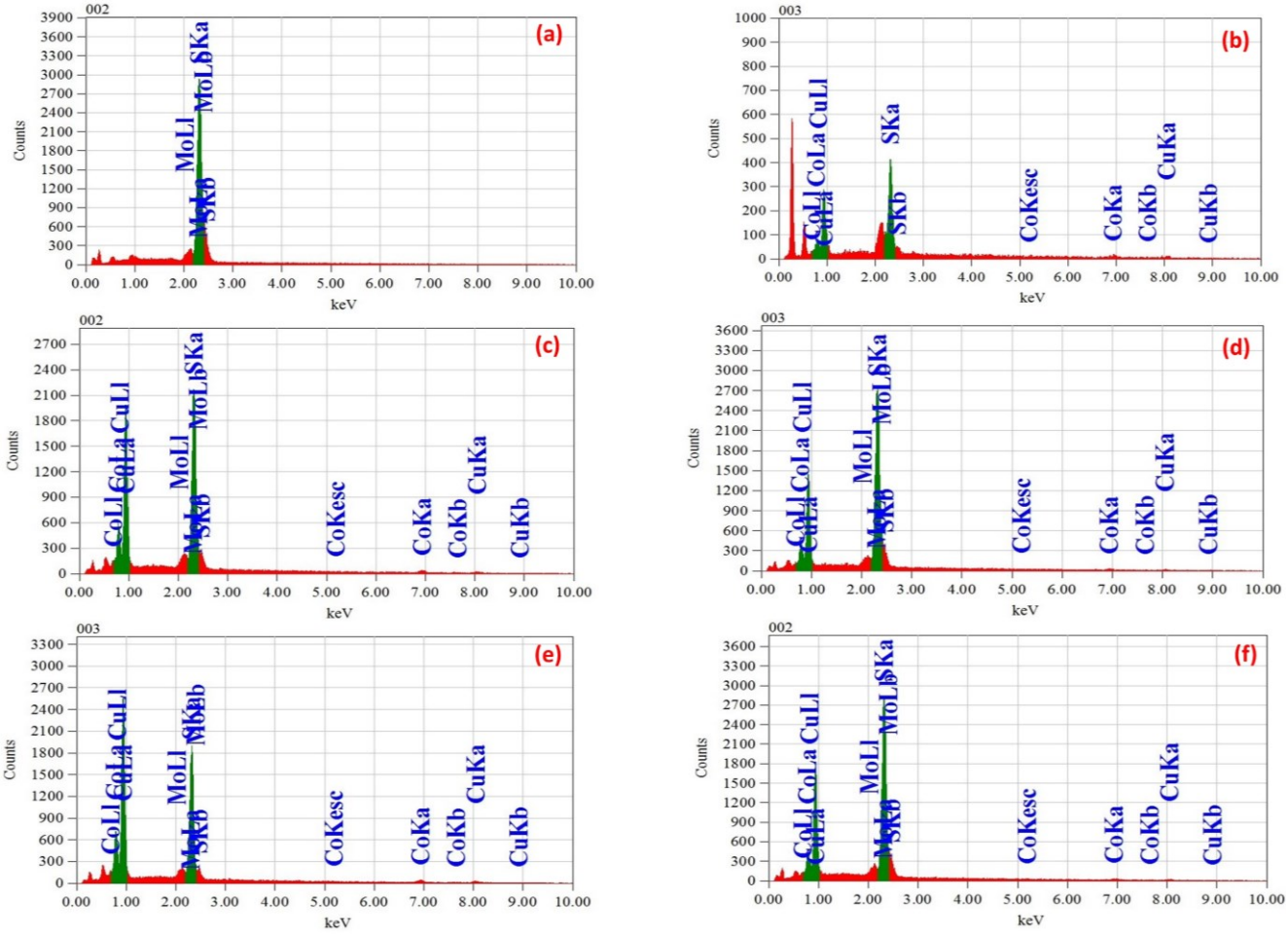


**Fig. S2.** EDX spectra of (a) $MoS_2$ nanosheets, (b) $CuCo_2S_4$, (c) $CuCo_2S_4$- $MoS_2$ (85:15), (d) $CuCo_2S_4$- $MoS_2$ (80:20), (e) $CuCo_2S_4$- $MoS_2$ (75:25) and (f) $CuCo_2S_4$ $MoS_2$ (70:30) nanocomposites.

## Note S4. Fourier-Transform Infrared Spectroscopy (FTIR) analysis

The functional group and molecular structure of the synthesized samples were analyzed by FTIR spectroscopy and the results are presented in Figure S3. Figure S3 depicts FTIR spectra in the 400 to 3000 $cm^{-1}$ range for $MoS_2$ NSs, CCS, and varying concentration of $MoS_2$ incorporated CCS-$MoS_2$ nanocomposites. In this fig., the weak peaks at 420 and 470 $cm^{-1}$ in the FTIR spectrum of $MoS_2$ NSs can be attributed to the vibration of Mo-S bonds, proving the formation of $MoS_2$ NSs [1,13]. In the FTIR spectrum of CCS, the peaks of around 623 and 1106 $cm^{-1}$ can be attributed to vibration of Cu-S and Co-S bonds, respectively, showing the formation of nanostructured CCS [1]. The peaks at about 1369 and 1736 $cm^{-1}$

| heightSample | Element | Mass (%) (theoretical) | Mass (%) (experimental) | Atom (%) (theoretical) | Atom (%) (experimental) |
|---|---|---|---|---|---|
| **$MoS_2$ nanosheets** | **Mo** | **59.94** | **52.15** | **33.33** | **29.55** |
| | **S** | **40.06** | **47.85** | **66.67** | **70.45** |
| **$CuCo_2S_4$** | **Cu** | **20.52** | **28.35** | **14.29** | **12.35** |
| | **Co** | **38.06** | **37.08** | **28.57** | **30.09** |
| | **S** | **41.42** | **44.57** | **57.14** | **57.56** |
| **$CuCo_2S_4$-$MoS_2$ (85:15)** | **S** | **41.28** | **42.34** | **58.57** | **59.03** |
| | **Mo** | **8.99** | **9.5** | **5** | **4.17** |
| **$CuCo_2S_4$-$MoS_2$ (80:20)** | **S** | **41.15** | **42.23** | **58.75** | **60.05** |
| | **Mo** | **11.99** | **12.41** | **6.67** | **6.45** |
| **$CuCo_2S_4$-$MoS_2$ (75:25)** | **S** | **41.08** | **42.09** | **59.52** | **60.36** |
| | **Mo** | **14.98** | **16.5** | **8.33** | **8.01** |
| **$CuCo_2S_4$-$MoS_2$ (70:30)** | **S** | **41.01** | **41.75** | **62.86** | **61.32** |
| | **Mo** | **17.98** | **19.11** | **10** | **9.85** |

**Table S2**. Mass and Atom percentages of elements in $MoS_2$ nanosheets, $CuCo_2S_4$ and $CuCo_2S_4$-$MoS_2$ nanocomposites as obtained via EDX and theoretical analysis.

appeared due to vibrations of $NO^{3-}$ asymmetric stretching (for nitrate precursor) and C=O stretching, respectively [14,15]. On the other hand, the peaks present at around 420 and 670 $cm^{-1}$ in the FTIR spectra of all the prepared CCS-$MoS_2$ nanocomposites were caused by the vibration of Mo-S and Cu-S-Mo bonds, respectively, and these peaks demonstrated that CCS-$MoS_2$ nanocomposites was successfully formed [1]. However, in the FTIR spectra of the prepared samples, the peak at around 2360 $cm^{-1}$ is due to the vibration of -OH functional groups from water molecules adsorbed from the product surface [16].

## Note S5. X-ray Photoelectron Spectroscopy (XPS) analysis

XPS was used to probe the chemical state and composition of the optimized CCS-$MoS_2$ (80:20) nanocomposite, with survey spectra in Figure S4. Figure 6(a) shows the spectrum of Cu 2p, where the two peaks of binding energy at 952.80 and 932.96 eV correspond to the $2p_{1/2}$ and $2p_{3/2}$ spin-orbit doublets of $Cu^+$, respectively [1,17,18]. Also, the two peaks of binding energy at 955.46 and 943.57 eV correspond to the $2p_{1/2}$ and $2p_{3/2}$ spin-orbit doublets of $Cu^{2+}$,

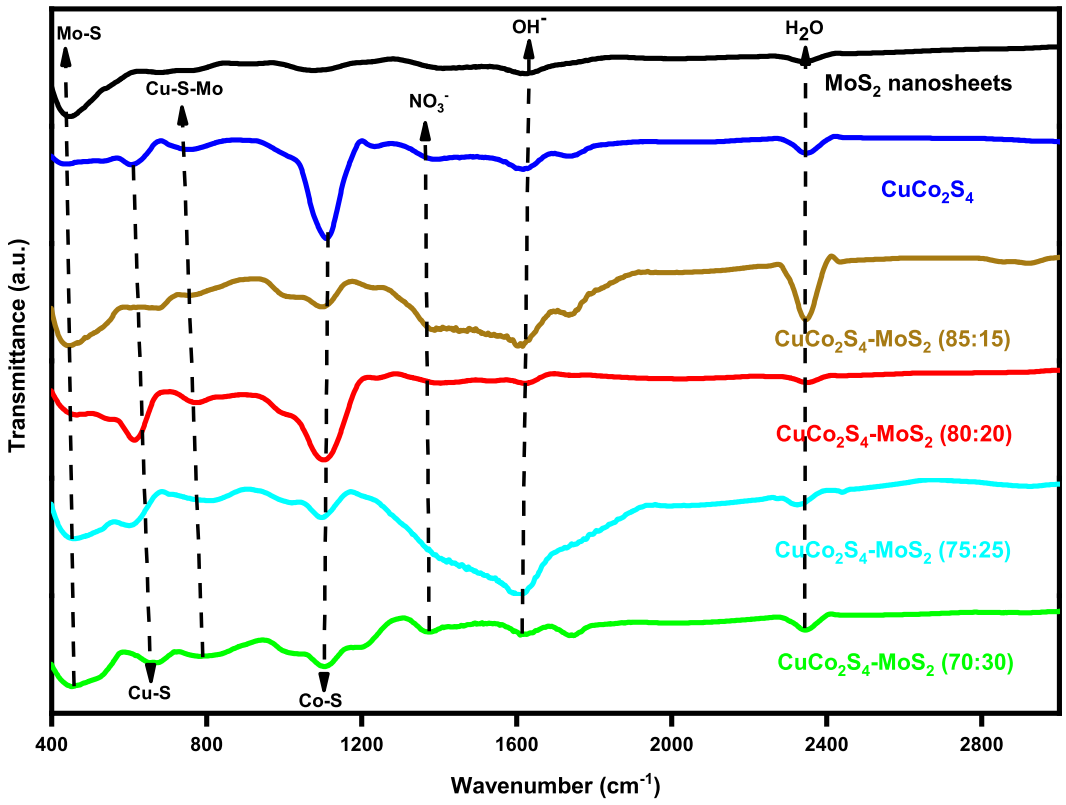


**Fig. S3.** FTIR spectra of $MoS_2$ nanosheets, $CuCo_2S_4$ and $CuCo_2S_4$-$MoS_2$ nanocomposites.

respectively [18] The energy difference of 19.84 eV between these two peaks is called the spin-orbit splitting energy, indicating the presence of CCS in the synthesized nanocomposite [1,18]. Also, the peaks at 963.04 and 935.18 eV are two satellite peaks, which are due to electron excitation to higher energy levels from the 2p core level of the $Cu^{2+}$ ion [18]. This can lead to redox reactions that increase the charge-carrying capacity of the nanocomposite. These two satellite peaks indicate that both $Cu^{+}$ and $Cu^{2+}$ ions co-exist in the sample which was absent in CCS-$MoS_2$ (90:10) nanocomposite [1]. Furthermore, enhancing the concentrations of $MoS_2$ in the sample leads to improve electrochemical performance compared to the previously reported CCS-$MoS_2$ (90:10) nanocomposite [1]. (Subsequent electrochemical analysis provided confirmation of this observation).

The high-resolution Co 2p orbital XPS spectrum is shown in Figure 6 (b). Whereas

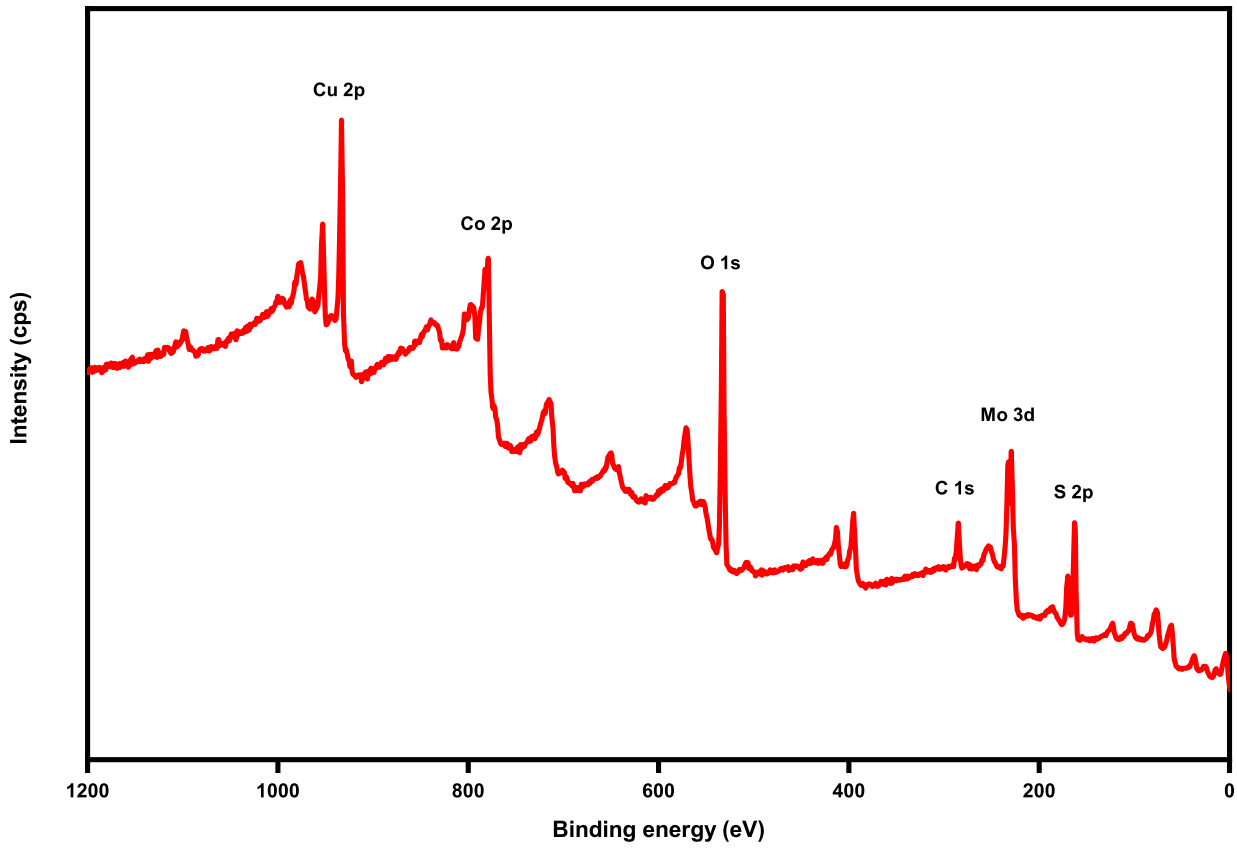


**Fig. S4.** XPS survey spectrum of $CuCo_2S_4$-$MoS_2$ (80:20) nanocomposite.

peaks at 793.61 and 778.74 eV binding energy are spin-orbit doublets of $2p_{1/2}$ and $2p_{3/2}$ orbitals of the octahedrally coordinated Co(II) ion, respectively [1,19]. On the other hand, two peaks obtained at 797.95 and 781.83 eV are spin-orbit doublets of $2p_{1/2}$ and $2p_{3/2}$ orbitals of octahedrally coordinated Co(III) ion, respectively [1,19]. The spin-orbit splitting energy separation of the Co 2p orbitals ($2p_{3/2}$ and $2p_{1/2}$) is 15 eV, revealing the sample's $Co^{2+}$ and $Co^{3+}$ oxidation states. Further, two satellite peaks of Co at 803.40 and 786.79 eV are observed due to elastic scattering processes (i.e. charge transfer), which may be conducive to more charge accumulation [1,19].

The high-resolution XPS spectrum of the Mo 3d orbital is shown in Figure 6(c), and it exhibits two peaks at binding energies of 229.57 and 232.74 eV, which are spin-orbit doublets of $3d_{3/2}$ and $3d_{5/2}$ orbitals of $Mo^{4+}$ in nanocomposite, respectively [20,21]. Which arises for the

transition of an electron from Mo's $3d_{3/2}$ and $3d_{5/2}$ orbitals to the valence band. The energy separation between these two peaks is 3.17 eV, reflecting the spin-orbit coupling interaction in the Mo atom. Additionally, the presence of $Mo^{6+}$ in the sample is indicated by the peak at 235.16 eV, which may be the result of $MoS_2$ being exposed to air [22]. The peak at 226.48 eV corresponds to the binding energy of the S 2s orbital of $MoS_2$ [20]. This results indicate the existence of Mo 3d and S 2s orbitals i.e. $MoS_2$ in nanocomposite.

The high-resolution XPS spectra of S 2p electrons is also shown in Figure 6 (d), where the peak at 162.31 eV and 161.47 belongs to the $2p_{3/2}$ orbital of $S^{2-}$ ligand and the peak at 163.47 eV fits into the $2p_{1/2}$ orbital of $S^{2-}$ or $S_2^{2-}$ ligand [20,23,24]. These two peaks indicate the presence of sulfide bonds in CCS and $MoS_2$ NSs which facilitate the electrochemical reaction. However, the peak at 169.75 eV is for residual $SO_4^{2-}$ species which is formed due to slightly oxidized S on the surface of the sample [25]. Surface analysis of the CCS-$MoS_2$ (80:20) nanocomposite revealed the presence of Cu, Co, S, and Mo, which supported the results obtained through EDX analysis. The position and symmetry of the peaks in the XPS spectra of S and Mo confirm the absence of monoclinic 1T-$MoS_2$ and the presence of hexagonal 2H-$MoS_2$ in the sample. Because the peak position of monoclinic 1T-$MoS_2$ is at slightly lower binding energy, which supports the results obtained through XRD analyses [8,26]. The XPS spectra of that nanocomposite show the presence of $Cu^{+}$, $Cu^{2+}$, $Co^{2+}$, $Co^{3+}$, $Mo^{4+}$, $Mo^{6+}$, $S^{2-}$ and $SO_4^{2-}$ ions which are favorable for redox reaction and thus the sample exhibits pseudocapacitive behavior, which helps enhance the charge storage capacity. These results suggest that the incorporation of different concentrations of $MoS_2$ with CCS will improve the electrochemical performance of CCS. Moreover, it will provide more active sites for electrolyte ion intercalation.

## Note S6. Nyquist plot analysis

In detail, $R_s$ (solution resistance) is the resistance of the electrolyte solution of the electrochemical cell which is encountered by the applied AC signal as it passes through the solution.

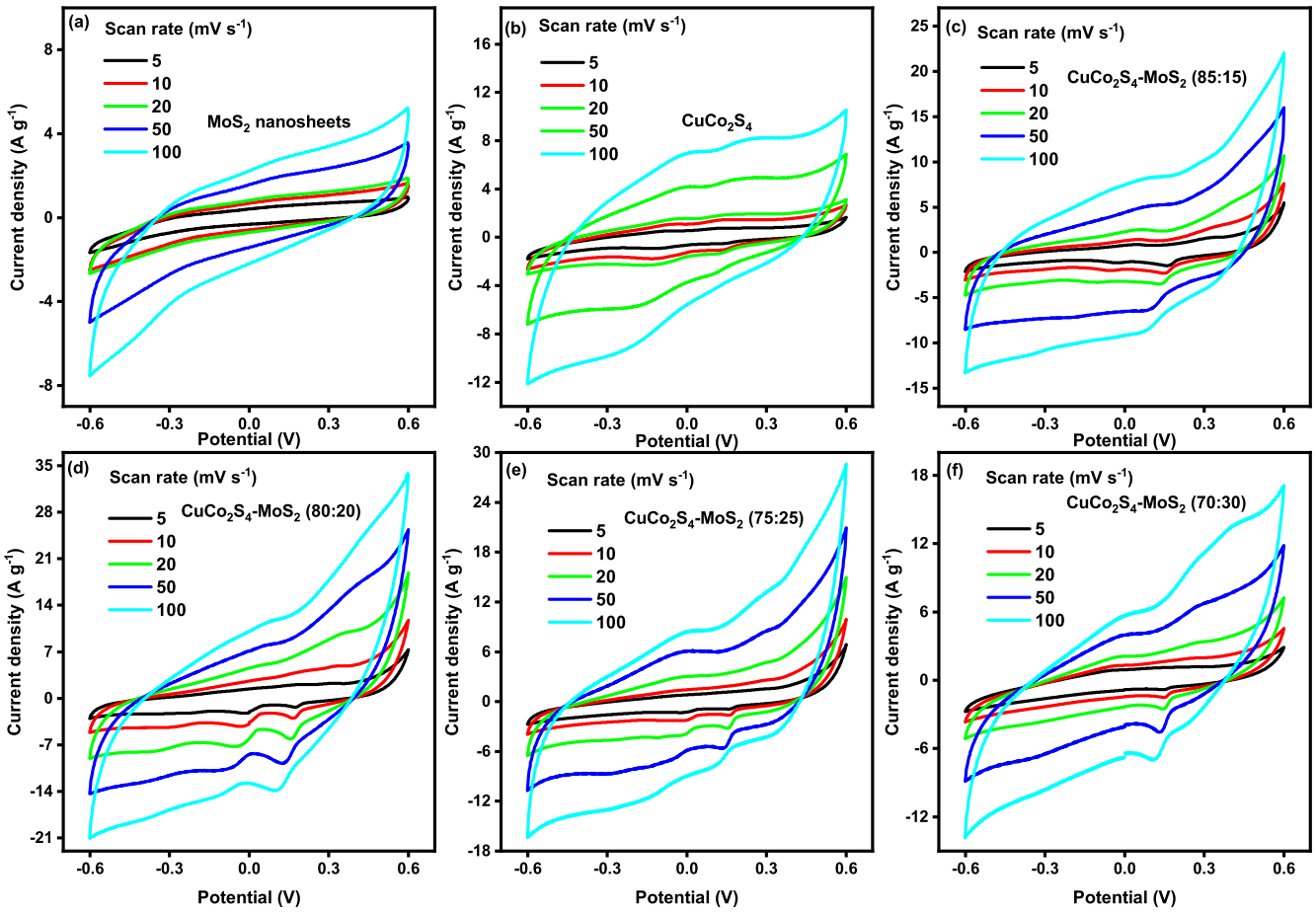


**Fig. S5.** CV curves of (a) $MoS_2$ nanosheets, (b) $CuCo_2S_4$, (c) $CuCo_2S_4$-$MoS_2$ (85:15), (d) $CuCo_2S_4$-$MoS_2$ (80:20), (e) $CuCo_2S_4$-$MoS_2$ (75:25) and (f) $CuCo_2S_4$-$MoS_2$ (70:30) nanocomposites in three-electrode system.

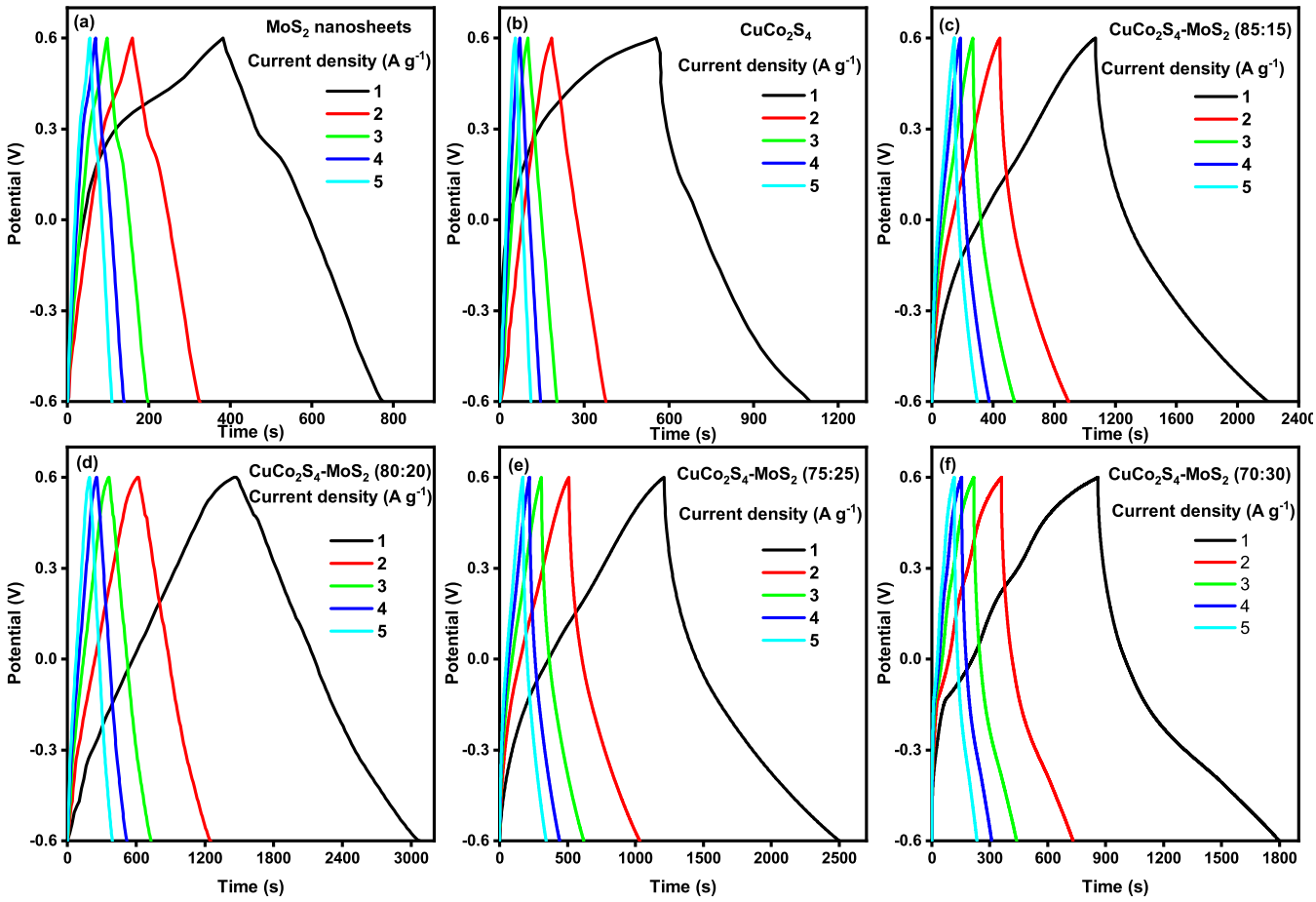


**Figure S6.** GCD curves of (a) $MoS_2$ nanosheets, (b) $CuCo_2S_4$, (c) $CuCo_2S_4$-$MoS_2$ (85:15), (d) $CuCo_2S_4$-$MoS_2$ (80:20), (e) $CuCo_2S_4$-$MoS_2$ (75:25) and (f) $CuCo_2S_4$-$MoS_2$ (70:30) nanocomposites in three-electrode system.

By analyzing the real part of the impedance (Z′) intercept in the high-frequency region of the impedance spectrum, $R_s$ is estimated. $R_{ct}$ ( charge transfer resistance) represents the resistance associated with the charge transfer process at the electrode-electrolyte interface, which is determined by measuring the diameter of the semicircular arcs in the Nyquist plot. $Z_w$ (Warburg impedance) relates to the diffusion of ions through the electrolyte towards the electrode surface or near the electrode-electrolyte interface. $Z_w$ is measured from the slope in the low-frequency or linear region of the Nyquist plot, and the value of this slope gives

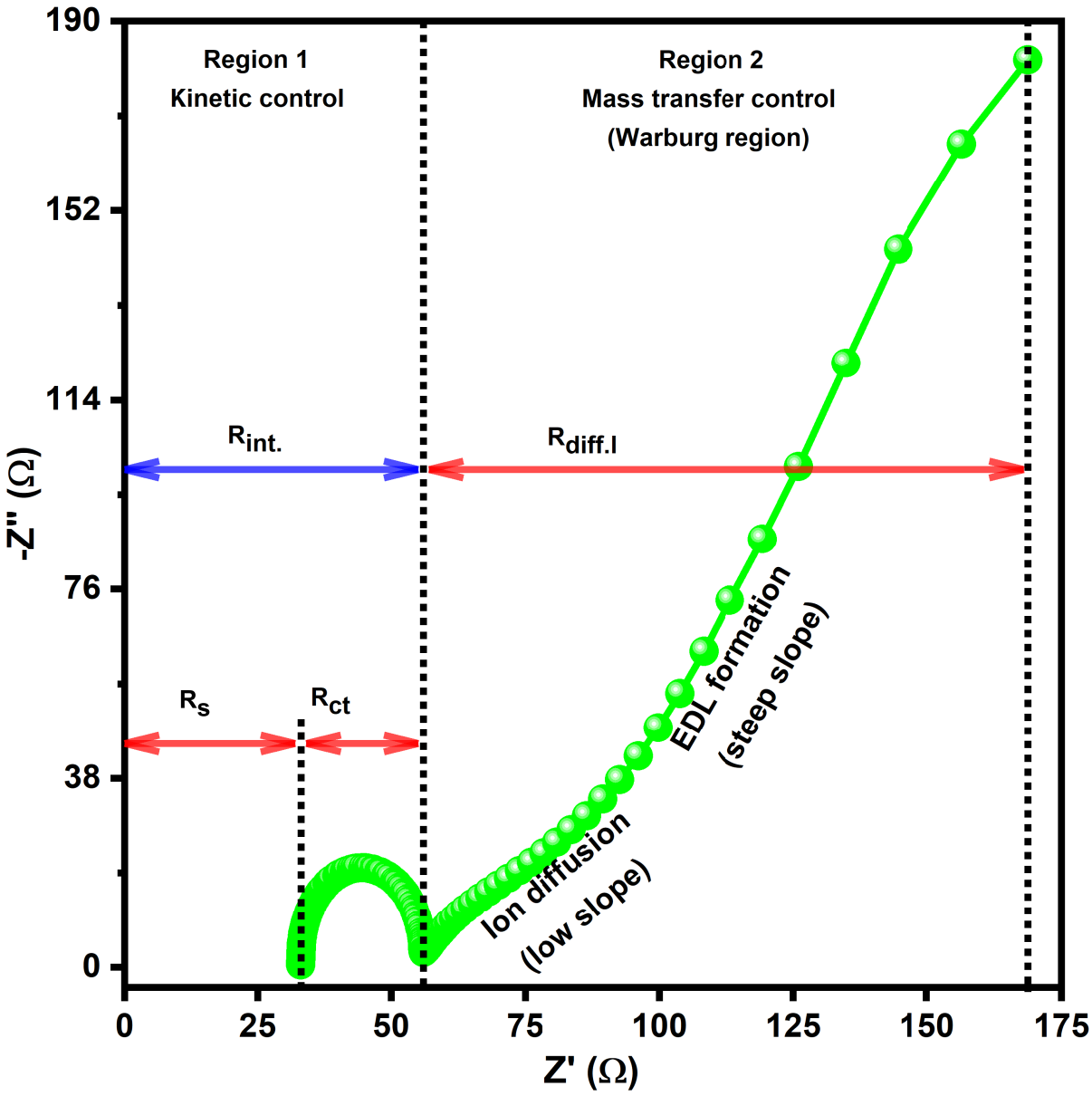


**Figure S7.** Nyquist plot of $CuCo_2S_4$ nanomaterial in three-electrode system.

information about the diffusion coefficient or the diffusion-limited behavior of the system. $C_{dl}$ represents the capacitance associated with the EDL formed due to the accumulation of charge at the electrode-electrolyte interface. $C_{dl}$ is usually observed as a semicircular curve in the Nyquist plot, representing capacitive behavior at intermediate frequencies. This can be estimated by analyzing the shape of the semicircular arc or by fitting the EIS data to the equivalent electrical circuit. $C_p$ (parallel capacitance) represents the additional capacitance contribution to the system beyond the EDL capacitance.$C_p$ was determined from the equivalent electrical circuit obtained by fitting the EIS data.

Figure S11 shows the Nyquist plot of CCS electrode to better analyze the parameters related to EIS. It consists of two regions namely region 1 (kinetic control region) and region 2 (Warburg region) [27]. The kinetic control region comprises a semicircle between points A and B at high frequencies. Here $R_{int.}$ is the internal resistance, which is the sum of $R_s$ and $R_{ct}$.

On the other hand, the mass transfer control region or Warburg region consists of a linear line with a steep and slow slope at median to low frequencies between points B and D. The slow slope seen at mid-frequency in the Nyquist plot is related to the ion diffusion process. At these frequencies, there is an interplay between the capacitive behavior (EDL) and the diffusion of ions in the electrolyte. The slow slope represents the impedance associated with limited ion diffusion at these frequencies. As the frequency decreases, the impedance gradually transits from capacitive behavior of the EDL to diffusion-limited behavior driven by ion transport in the electrolyte. On the other hand, the steep slope in the low-frequency region of the Nyquist plot is indicative of the formation of an EDL. This region is often referred to as the "capacitive region" of the Nyquist plot [27]. At low frequencies, there is sufficient time for charge redistribution within the EDL, resulting in significant changes in impedance. This steep slope represents the impedance associated with charging and discharging of the EDL. The total impedance of this region is called the diffuse layer impedance ($R_{diff.l}$) [27].

The impedance parameters were determined by fitting the EIS data (Nyquist plot) of the

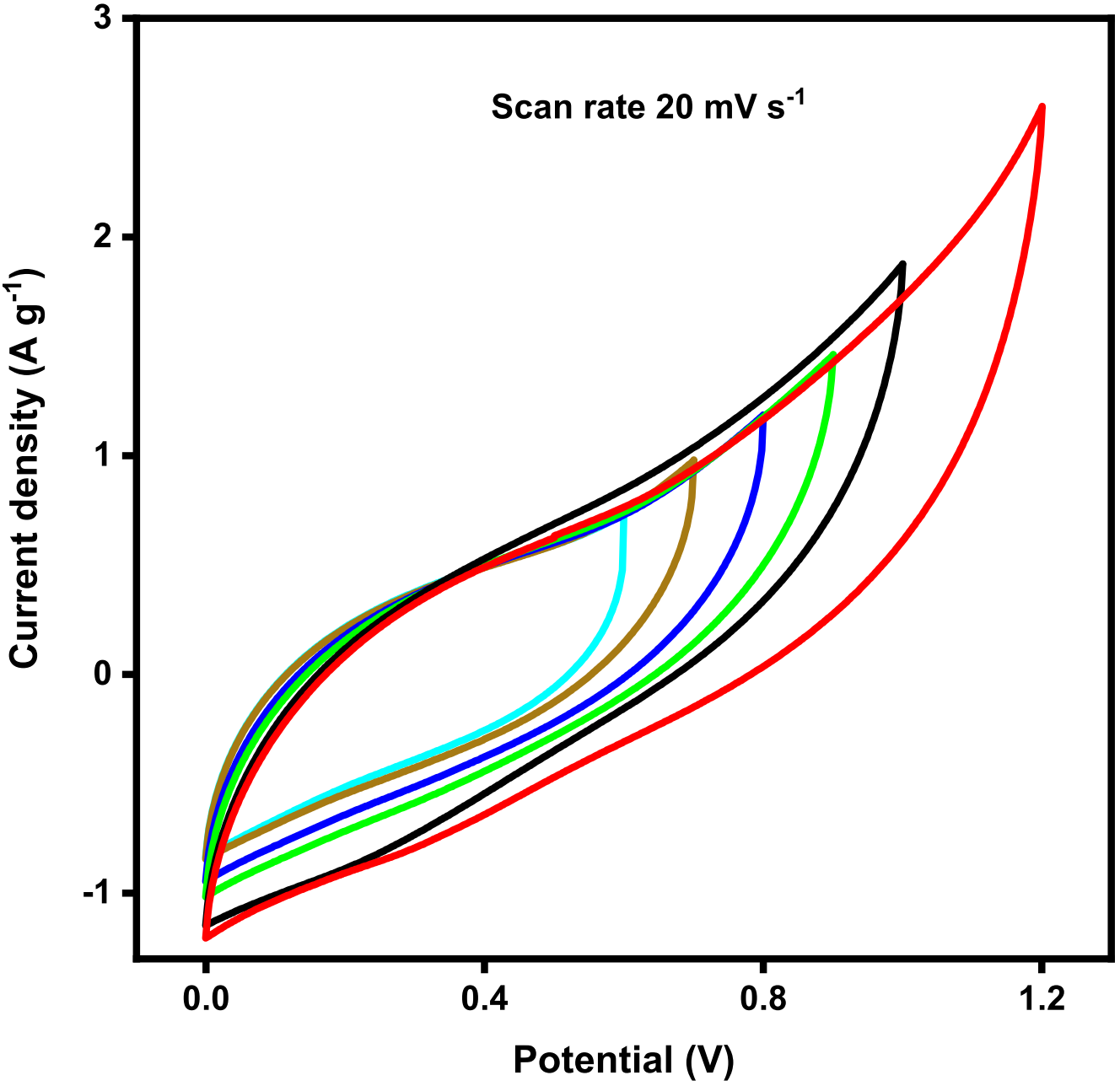


**Figure S8.** Potential window variation of $CuCo_2S_4$ nanomaterial electrode in symmetric two-electrode system.

**Table S3.** Values of $R_s$, $R_{ct}$, $C_{dl}$, $Z_W$ and $C_p$ in the three-electrode system obtained by fitting with an equivalent circuit.

| Sample | $R_s$ ($\Omega$) | $R_{ct}$ ($\Omega$) | $C_{dl}$ (F) | $Z_W$ ($\Omega$) | $C_p$ (F) |
|---|---|---|---|---|---|
| $MoS_2$ nanosheets | 18 | 3.79 | 0.00915 | 0.00231 | |
| $CuCo_2S_4$ | 33 | 22.95 | 0.06882 | 0.05698<br>0.00802 | 0.0521 |
| $CuCo_2S_4$-$MoS_2$ (85:15) | 11.20 | 13.52 | 0.01668 | 0.00321 | 0.00217 |
| $CuCo_2S_4$-$MoS_2$ (80:20) | 9.02 | 8.77 | 0.00824 | 0.00297 | 0.00184 |
| $CuCo_2S_4$-$MoS_2$ (75:25) | 10.09 | 13.33 | 0.00503 | 0.00353 | 0.00251 |
| $CuCo_2S_4$-$MoS_2$ (70:30) | 12.36 | 12.55 | 0.00273 | 0.00414 | 0.00612 |

synthesized samples to an equivalent electrical circuit.

**Table S4.** Values of $R_s$, $R_{ct}$, $C_{dl}$, $Z_W$ and $C_p$ in the symmetric two-electrode system obtained by fitting with an equivalent circuit.

| Sample | $R_s$ ($\Omega$) | $R_{ct}$ ($\Omega$) | $C_{dl}$ (F) | $Z_W$ ($\Omega$) | $C_p$ (F) |
|---|---|---|---|---|---|
| $MoS_2$ nanosheets | 29.68 | 0.005 | 0.002288 | 0.00462 | |
| $CuCo_2S_4$ | 90.6 | 60.3 | 0.017205 | 0.11396 | 0.1042 |
| $CuCo_2S_4$-$MoS_2$ (85:15) | 50.1 | 5.025 | 0.00417 | 0.01604 | 0.00642 |
| $CuCo_2S_4$-$MoS_2$ (80:20) | 47.1 | 40.02 | 0.00206 | 0.00642 | 0.00368 |
| $CuCo_2S_4$-$MoS_2$ (75:25) | 52.45 | 44.55 | 0.001258 | 0.00594 | 0.00502 |
| $CuCo_2S_4$-$MoS_2$ (70:30) | 64.8 | 50.905 | 0.000683 | 0.00706 | 0.01224 |

## Note S7. Charge Storage Mechanism

Here CCS-$MoS_2$ nanocomposite is used as anode and cathode material, 0.5 M neutral $Na_2SO_4$ as an electrolyte and Whatman filter paper as a separator. This separator prevents direct contact between the two electrodes, while the electrolyte connects them. When a voltage is applied to accumulate charge on the electrodes, the electrolyte solution is ionized ($Na^+$ and $SO_4^{2-}$) and ions from the solution flow towards the electrode surface. The negative ions ($SO_4^{2-}$) of the electrolyte flow towards the anode and the positive ions ($Na^+$) towards the cathode. Some of these ions are adsorbed on the electrode surface to form a layer of adsorbed ions known as Inner Helmholtz Plane (IHP). IHP is characterized by a high ion

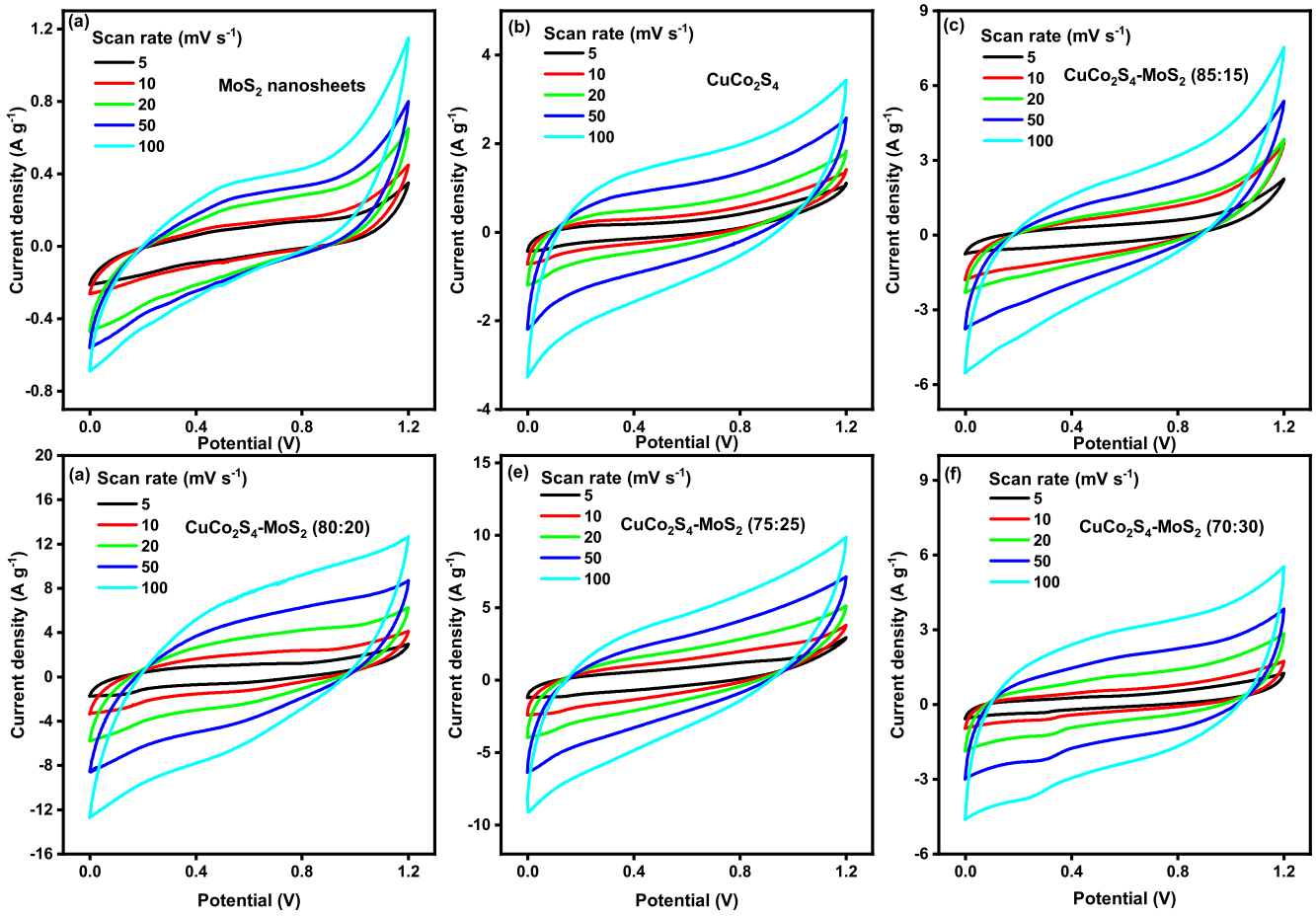


**Figure S9.** CV curves of (a) $MoS_2$ nanosheets, (b) $CuCo_2S_4$, (c) $CuCo_2S_4$-$MoS_2$ (85:15), (d) $CuCo_2S_4$-$MoS_2$ (80:20), (e) $CuCo_2S_4$-$MoS_2$ (75:25) and (f) $CuCo_2S_4$-$MoS_2$ (70:30) nanocomposites in symmetric two-electrode system.

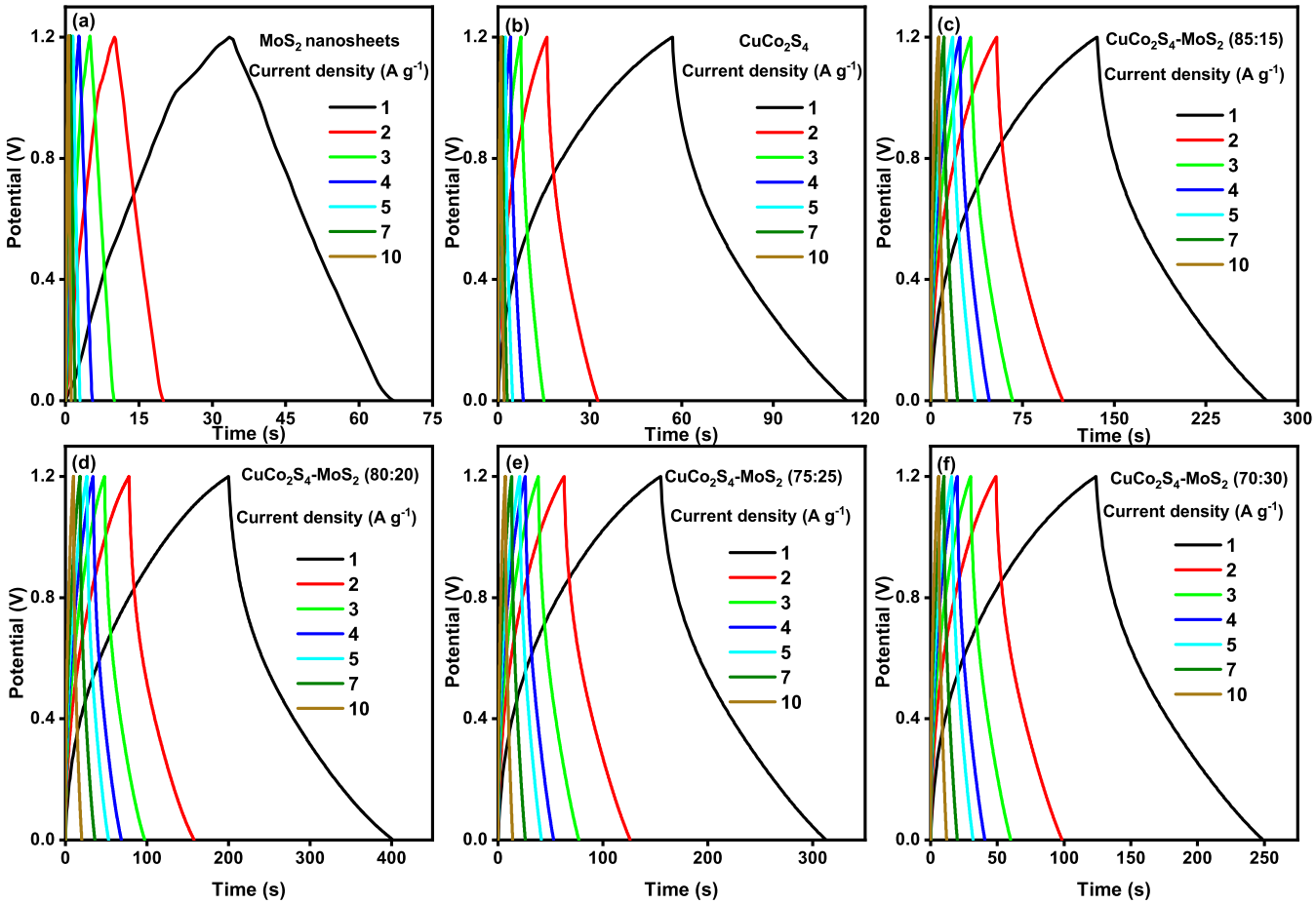


**Figure S10.** GCD curves of (a) $MoS_2$ nanosheets, (b) $CuCo_2S_4$, (c) $CuCo_2S_4$-$MoS_2$ (85:15), (d) $CuCo_2S_4$-$MoS_2$ (80:20), (e) $CuCo_2S_4$-$MoS_2$ (75:25) and (f) $CuCo_2S_4$-$MoS_2$ (70:30) nanocomposites in symmetric two-electrode system.

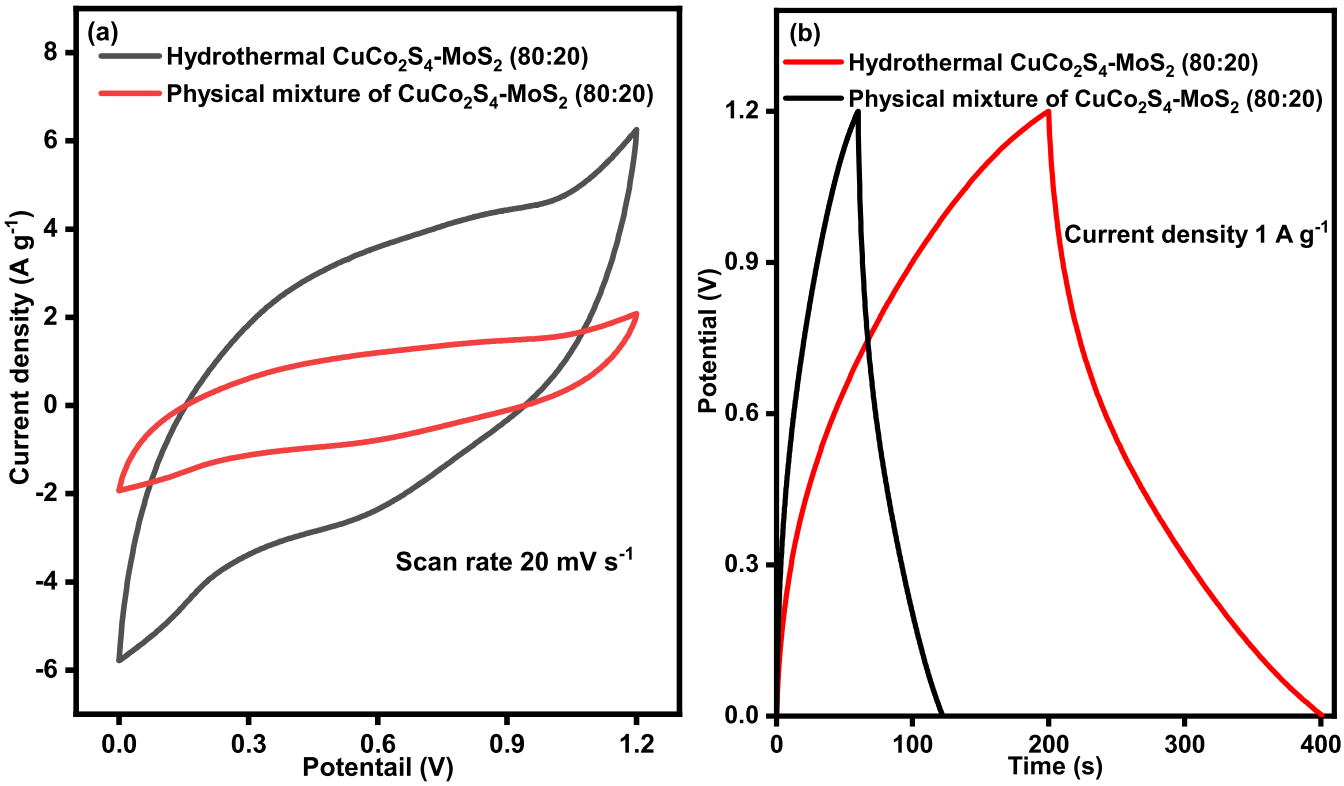


**Figure S11.** Comparison of the electrochemical behavior of physically and hydrothermally mixed $CuCo_2S_4$ (80:20) nanocomposite (a) CV curves and (b) GCD curves evaluated in symmetric two-electrode system.

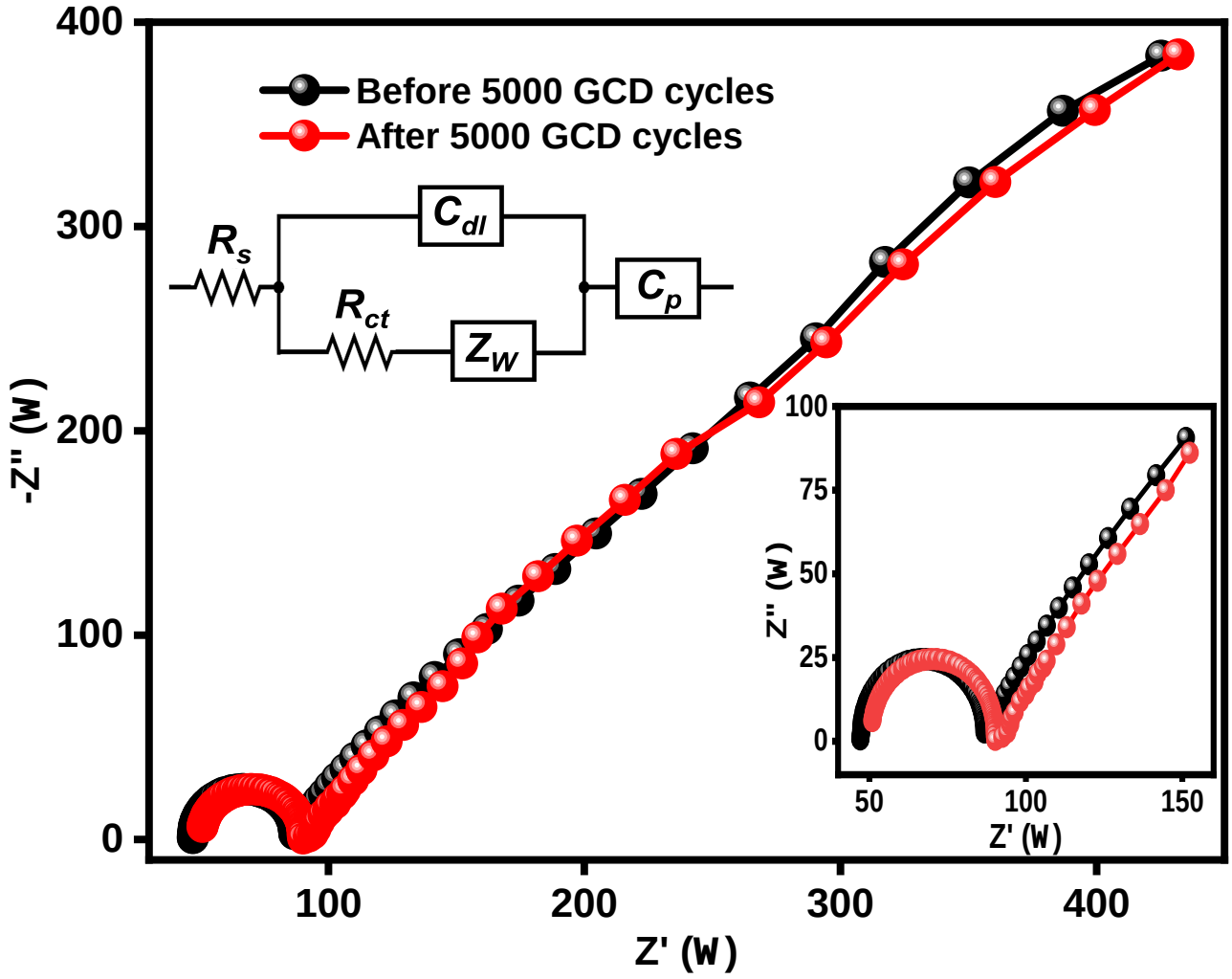


**Figure S12.** Comparison of the Nyquist plot of $CuCo_2S_4$-$MoS_2$ (80:20) nanocomposite before and after of 5000 GCD cycles evaluated in symmetric two-electrode system.

concentration and strong electrostatic interactions between adsorbed ions and the electrode surface. This layer is composed of highly ordered solvent molecules and ions due to strong electrostatic interactions. These adsorbed ions play an important role in the formation of EDL and reversible redox reactions. Outside of the IHP is the Outer Helmholtz Plane (OHP), which is composed of ions that are not as strongly bound to the electrode surface as the adsorbed ions in the IHP. It extends further away from the electrode surface and acts as an intermediate region between the electrode surface and the bulk electrolyte. The combination of IHP and OHP leads to the formation of EDL. Adsorbed ions tightly bound to the IHP contribute to the physical separation of charge, creating a high-capacitance region near the electrode surface. Overall, the combination of IHP and OHP layers at the electrode-electrolyte interface leads to the formation of an EDL, which stores electrical energy by creating a high-capacitance region near the electrode surface. CCS-$MoS_2$ nanocomposite can intercalate electrolytes between their layers which are called intercalated ions. These ions form part of the pseudocapacitive behavior of the system and contribute to the overall charge storage capacity by undergoing reversible redox reactions. The diffuse layer, which extends from the OHP to the bulk electrolyte solution, contains ions that are more mobile and less affected by the electrode surface. It acts as a transition zone between the electrode surface and the bulk electrolyte, allowing ion transport. The diffuse layer itself does not directly contribute to the pseudocapacitance or EDLC, but it plays an important role in establishing and maintaining the conditions necessary for the formation of the EDL and the occurrence of pseudocapacitive reactions. In the case of EDL, when a positive potential is applied to the electrode, cations from the bulk electrolyte are attracted to the negatively charged electrode, while anions are repelled. This results in the formation of a layer of positive charge (cations) near the electrode surface, which contributes to the formation of EDL. Conversely, during extraction, the ions redistribute, returning to their equilibrium position in the bulk electrolyte. On the other hand, the diffuse layer enables ion transport from the bulk electrolyte to the electrode surface, facilitates the participation of ions and

supports the redox reaction by maintaining their availability, thereby contributing to the pseudocapacitive charge storage process.

## Notes and references


1 S. Hasan, A. H. Reaz, S. Das, C. K. Roy and M. A. Basith, *J. Mater. Chem. C*, 2022, **10**, 7980–7996.

2 A. M. Tama, S. Das, S. Dutta, M. D. I. Bhuyan, M. N. Islam and M. A. Basith, *RSC Adv.*, 2019, **9**, 40357–40367.

3 C. K. Roy, S. S. Shah, A. H. Reaz, S. Sultana, A.-N. Chowdhury, S. H. Firoz, M. H. Zahir, M. A. Ahmed Qasem and M. A. Aziz, *Chem. Asian J.*, 2021, **16**, 296–308.

4 Y. Li, G. Zhu, X. Xu, L. Chen, T. Lu, J. P. Hill, L. Pan and Y. Yamauchi, *Small Structures*, 2022, **3**, 2200015.

5 X. Lei, S. Ge, Y. Tan, Z. Wang, J. Li, X. Li, G. Hu, X. Zhu, M. Huang, Y. Zhu and B. Xiang, *ACS Appl. Mater. Interfaces*, 2020, **12**, 9158–9168.

6 K. Makgopa, P. M. Ejikeme, C. J. Jafta, K. Raju, M. Zeiger, V. Presser and K. I. Ozoemena, *J. Mater. Chem. A*, 2015, **3**, 3480–3490.

7 S. A. Melchior, K. Raju, I. S. Ike, R. M. Erasmus, G. Kabongo, I. Sigalas, S. E. Iyuke and K. I. Ozoemena, *J. Electrochem. Soc.*, 2018, **165**, A501.

8 B. A. Ali, A. M. A. Omar, A. Khalil and N. K. Allam, *ACS Appl. Mater. Interfaces*, 2019, **11**, 33955–33965.

9 R. Wang, S. Wang, X. Peng, Y. Zhang, D. Jin, P. K. Chu and L. Zhang, *ACS Appl. Mater. Interfaces*, 2017, **9**, 32745–32755.

10 B. A. Ali, O. I. Metwalli, A. Khalil and N. K. Allam, *ACS Omega*, 2018, **3**, 16301–16308.

11 S. Ardizzone, G. Fregonara and S. P. Trasatti, *Electrochim. Acta*, 1990, **35**, 263–267.

12 Z.-H. Huang, T.-Y. Liu, Y. Song, Y. Li and X.-X. Liu, *Nanoscale*, 2017, **9**, 13119–13127.

13 N. Chaudhary, D. Avasthi, Abid and S. K. Islam, *Sens. Actuator A* Phys., 2018, **277**, 190–198.

14 M. K. Trivedi and A. B. Dahryn Trivedi, *J. Chromatogr. Sep. Tech.*, 2015, **06**.

15 M. Mariappan, G. Madhurambal, B. Ravindran and S. C. Mo- jumdar, *J. Therm. Anal. Calorim.*, 2011, **104**, 915–921.

16 M. Aghaei, M. Imani and A. Tadjarodi, *Chem. Proc.*, 2020, **3**, 51–51.

17 S. Zhao, Y. Wang, Q. Zhang, Y. Li, L. Gu, Z. Dai, S. Liu, Y.-Q. Lan, M. Han and J. Bao, *Inorg. Chem. Front.*, 2016, **3**, 1501– 1509.

18 H. Sun, O. A. Zelekew, X. Chen, Y. Guo, D.-H. Kuo, Q. Lu and J. Lin, *RSC Adv.*, 2019, **9**, 31828–31839.

19 L. Xu, G. Pan, C. Yu, J. Li, Z. Gong, T. Lu and L. Pan, *Inorg. Chem. Front.*, 2023, **10**, 1748–1757.

20 F. Huang, R. Meng, Y. Sui, F. Wei, J. Qi, Q. Meng and Y. He, *J. Alloys Compd.*, 2018, **742**, 844–851.

21 E. G. da Silveira Firmiano, A. C. Rabelo, C. J. Dalmaschio, A. N. Pinheiro, E. C. Pereira, W. H. Schreiner and E. R. Leite, *Adv. Energy Mater.*, 2013, **4**, 1301380.

22 J. Duchet, v. E. Oers, V. Beer and R. R. Prins, *J. Catal.*, 1983, **80**, 386–402.

23 J. Qi, X. Liu, Y. Sui, Y. He, Y. Ren, Q. Meng, F. Wei and X. Zhang, *J. Mater. Sci. Mater. Electron.*, 2018, **30**, 667–676.

24 D. Escalera-López, Y. Niu, S. J. Park, M. Isaacs, K. Wilson, R. E. Palmer and N. V. Rees, *Appl. Catal. B*, 2018, **235**, 84–91.

25 H. Wang, Y. Song, Y. Zhao, Y. Zhao and Z. Wang, *Nanomaterials*, 2022, **12**, 3104–3104.

26 D. Sun, D. Huang, H. Wang, G.-L. Xu, X. Zhang, R. Zhang, Y. Tang, D. A. EI-Hady, W. Alshitari, A. S. Al-Bogami, K. Amine and M. Shao, *Nano Energy*, 2019, **61**, 361–369.

27 B.-A. Mei, O. Munteshari, J. Lau, B. Dunn and L. Pilon, *J. Mater. Chem. C*, 2017, **122**, 194–206.